Journal of Materials Chemistry A

Accepted Manuscript

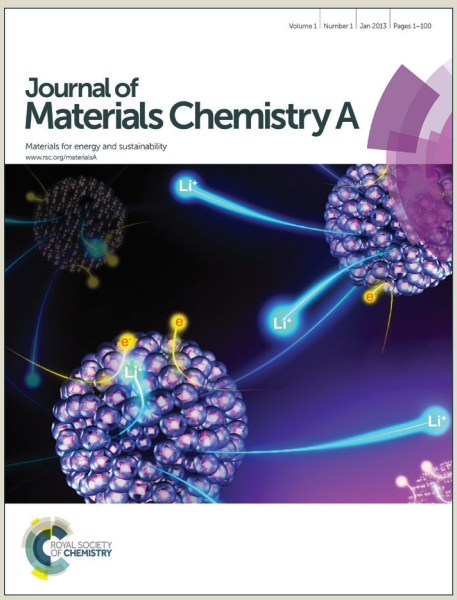

ROYAL SOCIETY OF CHEMISTRY

www.rsc.org/materialsA

Origin of Anomalous Large Reversible Capacity for SnO_2 conversion reaction

Kazuaki Kisu,[1] Minami Iijima,[1] Etsuro Iwama,[1] Morihiro Saito,[1] Yuki Orikasa,[2] and Wako Naoi,[3] Katsuhiko Naoi*[1,3,4]

[1]*Department of Applied Chemistry, Tokyo University of Agriculture & Technology, 2-24-16 Naka-cho, Koganei, Tokyo 184-8558, Japan*
**E-mail: k-naoi@cc.tuat.ac.jp*

[2]*Graduate School of Human and Environment Studies, Kyoto University, Yoshida-nihonmatsu-cho, Sakyo-ku, Kyoto 606-8501, Japan*

[3]*Division of Art and Innovative Technologies, K & W Inc., 1-3-16-901 Higashi, Kunitachi, Tokyo 186-0002, Japan*

[4]*Advanced Capacitor Research Center, Tokyo University of Agriculture & Technology, 2-24-16 Naka-cho, Koganei, Tokyo 184-8588, Japan*

Abstract

Single-nanocrystalline SnO_2 (2-4 nmϕ) particles hyperlinked and encapsulated within hollow-structured carbon black (Ketjen Black (KB), typically 40 nmϕ) were prepared using our original *in-situ* ultracentrifugation (UC) materials processing technology (UC process). Ultracentrifugation at 75,000G induces an *in-situ* sol-gel reaction that brings about optimized hyperlinks between limited-size SnO_2 nanocrystals and microcrystalline graphitic carbons of KB. Efficient entanglement and nanonesting has been accomplished by simultaneous nanofabrication and nanohybridization in the UC process, specifically at a ratio of SnO_2/KB = 45/55. This composite exhibited a reversible capacity of 837 mAh g^{-1} per composite, equivalent to 1444 mAh g^{-1} (per pure SnO_2 after subtracting of capacity attributed to KB in the composite) for remarkably many cycles, over 1200. Such high performance in regard to both capacity and cyclability has never been attained so far for SnO_2 anode materials. The reversibility of the changes in Sn valence state (defined as "formal valence state" in the manuscript) from Sn(2.9+) to Sn(4.4-) was demonstrated by *in-situ* XAFS measurement during the lithiation-delithiation process. Peculiar nanodots of typically 2–4 nm that look like single-crystal SnO_2/carbon core-shell structures were found for the optimized dose ratio (45/55) in the HRTEM observation. After 10 cycles, all the materials showed complete encapsulation of the same-sized nanoparticles, which were covered and nested within the KB matrix and an electrolyte-derived polymeric film. These results indicate that the initially prepared SnO_2/KB composites were transformed into a new species, represented as $Li_xSnO_{1.45}$ (x: 0–7.3), which shows perfect reversibility and cyclability. This species can exchange a total of 7.3 electrons, including 2.9 electrons for the conversion reaction (1–2 V) and 4.4 electrons for the subsequent alloying

process (0–1 V).

Introduction

Lithium-ion batteries (LiBs) are the most widely used type of rechargeable electrochemical energy storage device because of their high volumetric energy density and excellent service life. However, their energy and power capabilities are still insufficient to meet the demands of consumer electronics and, more importantly, electronic automotive applications.[1] Although graphite remains the most widely used anode material in commercial LiBs, it cannot meet the requirements for high-capacity LiBs, because its theoretical value is only 372 mAh g^{-1}, which has already nearly been reached.[2] Thus, alternative high-capacity anode materials are required and have been vigorously investigated. For example, metal oxides such as V_2O_3,[3] MnO,[4] Mn_3O_4,[5] Fe_2O_3,[6] Fe_3O_4,[7] CoO,[8] Co_3O_4,[9] NiO,[10] CuO,[11] ZnO,[12] MoO_3,[13] SnO_2,[14] and SiO_2,[15] which act as anode materials undergoing conversion reactions, have attracted intense interest because of their high theoretical capacities (700–1500 mAh g^{-1}), regardless of some issues such as inappropriate voltage range (from 0 to 2~4 V *vs.* Li/Li^+) and initial irreversible capacity for practical application of LiBs. SnO_2 is the one of the most well-characterized systems among those conversion anodes because of its high theoretical capacity of 1494 mAh g^{-1} (quadruple of the theoretical capacity of graphite) delivered in a relatively lower operation voltage range of 0–2 V.[16] Furthermore, SnO_2 is inexpensive, exhibits low toxicity, and is environmentally benign.[17]

It is generally understood that SnO_2 undergoes two types of redox reactions in which 8.4 electrons and Li^+ are theoretically exchanged in total.[18] First, the conversion reaction ($SnO_2 + 4Li^+ + 4e^- \rightarrow Sn + Li_2O$) occurs at 1.54 V *vs.* Li/Li^+ during the lithiation process. This

conversion reaction was considered as completely irreversible until early beginning of 2000[19-21], while some of recent reports suggest that it is partially reversible[22-23]. The subsequent alloying process ($Sn + 4.4Li^+ + 4.4e^- \rightarrow Li_{4.4}Sn$) occurs over a wider voltage range of 0.3–0.7 V and is recognized to be more reversible.[24] One serious problem with the alloying reaction is the drastic volumetric expansion (max. 359%) occurring during the complete alloying from Sn(0) to the fully lithiated state of $Li_{4.4}Sn$.[18] Such a large volume expansion[19,24,25] induces surface cracking and damage to the whole electrode, including both the tin (SnO_2) and the carbon conductive agents (e.g., acetylene black). This may cause a loss of electrical contact between SnO_2 and the carbon network as well as between the electrode and the current collector. Another issue is the pulverization associated with the large volumetric increase up to, typically, 100 cycles.[26-28] Winter *et al.*[19] clearly demonstrated such cracking by performing careful SEM observations during the alloying process. Two important approaches have been proposed to overcome these pulverization problems. One is to use nanosized SnO_2 to reduce the absolute volume changes of the reactive phases, and the other is to design a stabilized multiphase composition[29] or microstructure in which nanoscale SnO_2 is finely dispersed in a well-accommodated neighboring matrix that allows smooth lithiation. Several major attempts have been made to improve the cycling performance of SnO_2 up to around 200 cycles.[30] Among these approaches, "nanocompounding," in which "nanofabrication" of the SnO_2 and "nanocompositing" with carbon material are achieved simultaneously, has been particularly promising. The nanofabricated SnO_2 can be prepared using either sol-gel or hydrothermal methods with $Sn(II)Cl_2$[31] or $Sn(VI)Cl_4$[32] as the starting material. Furthermore, various organic compounds such as glucose,[33] phenol formaldehyde,[34] ethylene glycol,[35] and sucrose[36] have been examined

as carbon sources for multifunctional nanocompositing agents. Carbon nanotubes[37,38] and graphene oxide[39,40] have also been examined as a more effective carbon matrix. Nanocompounding normally yields SnO_2 particles (5 to 10 nm) smaller than those in commercially available reagent-grade SnO_2 (primary particle size = 100 nm; Aldrich). This nanocompounding certainly prolonged the cycle lifetimes, somewhat, to around 200 cycles, but a long cycling life over 200 cycles had not been achieved. The factors contributing to such short cycle lifetimes are considered to be (1) aggregation of the SnO_2 nanoparticles over 200 cycles and (2) possible decomposition of the electrolytes catalyzed by the reduced Sn(0) nanoparticles. Recently, there are two reports on the SnO_2/graphene composites, which show a high reversible capacity of 800-1350 mAh g^{-1} over 500-1000 cycles.[41,42] Such a long cycle life was achieved owing to the encapsulation of SnO_2 nanoparticles (4-5 nm prepared *via.* hydrothermal method) by graphene 2D layers, which limits aggregation of tin nanoparticles generated during lithiation.

In our case, in order to further prolong the cycle lifetimes of SnO_2, a complete encapsulation of the single nanoscale SnO_2 crystals within hollow-structured carbon black (Ketjen Black; KB) was achieved by a unique in-situ materials processing technique under ultracentrifugation (75,000 G) called UC treatment.[43,44] KB is a type of carbon black, possesses hollow sphere structure, and consists of disordered microcrystalline graphitic carbons.[45,46] Using this UC treatment, nanosized (ca. 2 nm) hydrous RuO_2/KB composite was successfully prepared.[43] The UC treatment drives an *in-situ* sol-gel reaction generating nanosized (< 5 nm) SnO_2 particles that are hyperdispersed and confined within the KB matrix. In the present study, we chose SnO_2 as a model material to dealt with the conversion essentials. We will describe the optimally dispersed and encapsulated nanophase crystalline SnO_2 (nc-SnO_2)/carbon composite exhibiting

a highly reversible capacity of 837 mAh g^{-1} up to >1200 cycles. Detailed evaluation of the structural features and electrochemical properties of the UC-treated nc-SnO_2/KB was also performed to propose a new mechanism that renders the conversion reaction highly reversible for prolonged cycle lifetimes.

Experimental

Materials. We first used Sn(II)$Cl_2 \cdot 2H_2O$ (Kanto Chemical Inc.) as a source of SnO_2 and a hollow-structured Ketjen Black (KB; EC600JD, Ketjen Black International Company) with 50 nm primary particles with a specific surface area (SSA) of 1270 m^2 g^{-1} as a carbon matrix to entangle with the growing nanoscale SnO_2. 6 M HCl aq. (Wako Pure Chemicals) was added to the starting solution to enhance the dissolution of Sn(II)$Cl_2 \cdot 2H_2O$ prior to the UC treatment, and 1 M NaOH aq. (Wako Pure Chemicals) was used to drive sol-gel process via hydration and polycondensation. Distilled water (17 MΩ cm) was used as a medium for the entire preparation scheme.

Preparation of nc-SnO_2/KB Composite under UC Treatment. *In-situ* synthesis of the nc-SnO_2 and its simultaneous nanohybridization with hollow-structured carbon black was carried out by performing UC treatment.[43,44] A transparent starting solution was obtained after $SnCl_2 \cdot 2H_2O$ and 1 mL of 6 M HCl aq. was mixed in 33 mL of distilled water. Various amounts of KB were then mixed in the solution under 5 min of ultrasonication to obtain a uniform premixture. The first UC process was carried out on this premixture for 5 min to obtain the perfect dispersion of Sn^{2+} and KB. In this process, the Sn^{2+} can attach uniformly on the surface

of the disaggregated primary particles of KB. After the addition of 17 mL of 1 M NaOH aq., the second UC treatment was performed for 2 min under hyperagitation at 75,000G. The second UC process induces the hydrolysis reaction in a controlled manner to achieve *in-situ* nucleation of the SnO_2 polynuclear precursors on KB. With this two-step UC process, the obtained particle size is well-controlled and is even smaller than the mean sizes reported previously.[43] The resultant solution with a dark precipitate consisting of precursor composites was filtered, washed with distilled water several times, and then dried at 180°C *in vacuo* for 12 h.

Physicochemical Characterizations of the nc-SnO_2/KB Composite. The detailed nanostructure of the composites was characterized by high-resolution transmission electron microscopy (HRTEM, Hitachi H9500 model) to evaluate the particle size distribution of the nc-SnO_2 and the disordered structure of the microcrystalline graphite of KB. X-ray diffraction (XRD, Rigaku SmartLab) measurements were performed to characterize the crystalline structure of the nc-SnO_2/KB in the composite. In order to characterize the stoichiometry of the composites, thermal analysis was performed under a synthetic air atmosphere (O_2 : 20%, N_2 : 80%) using a thermogravimetry differential thermal analyzer (TG/DTE, Seiko Instruments TG/DTA6300).

Electrochemical and Battery Characterizations of nc-SnO_2/KB Composites. The half-cell was assembled with a Li metal electrode and a nc-SnO_2/KB electrode using a 2032 coin-type cell. The electrolyte was a mixture of ethylene carbonate (EC) and diethyl carbonate (DEC) containing 1.0 M lithium hexafluorophosphate ($LiPF_6$) as an electrolyte salt. The nc-SnO_2/KB

electrode was prepared by mixing the composite (85% by mass), acetylene black (AB, Denka Acetylene Black HS-100, provided from DENKI KAGAKU KOGYO K.K (DENKA); 5%), and polyvinylidene difluoride (PVdF; 10%) in *N*-methyl pyrrolidone (NMP). The mixture was coated on Cu foil (current collector) and dried at 150 ℃ *in vacuo* for 3 h. The thickness of the nc-SnO_2/KB electrode was controlled to ca. 20 μm. The average loading mass of active material was ca. 0.5 mg cm^{-2}. Charge-discharge tests were performed in CC-CV(lithiation) and CC (delithiation) mode between 0.0 and 2.0 V at a current density of 0.2 C-rate assuming 1 C-rate is 1494 mAh g^{-1}.

***In-Situ* XAFS Measurements.** *In-situ* X-ray adsorption fine structure (XAFS) measurements at the Sn K-edges were performed in a fluorescence mode on the composite samples at the beam line BL14B2[47] of the synchrotron radiation facility Spring-8 (Hyogo, JAPAN). The fluorescence signals were collected by a 19-element solid-state detector. Using this SnO_2/KB composite electrode, laminate-type two-electrode cells were assembled with lithium metal foil. Charge-discharge tests were performed on the assembled laminate cell in the voltage range of 0–2.0 V during the 1st and 10th cycles at a rate of 0.2 C. The XAFS spectra were recorded at an equilibrium state following a rest period of 20 min at each voltage. The obtained XAFS spectra were analyzed with the spectral fitting software REX2000 (Rigaku Corp.) to evaluate the ratio of Sn species with different valance states such as Sn0 (Sn metal), Sn4+ (SnO_2), Sn4.4- ($Li_{4.4}Sn$).

Results and discussion

We varied the Sn dosing ratio from 30 wt% to 90 wt% in an attempt to synthesize SnO_2/KB nanocomposites with the maximum SnO_2 contents. The crystalline structure of the obtained SnO_2/KB composite was confirmed by XRD analysis. A dosing ratio of over 90 wt% gave strong and sharp XRD signals for SnO along with broad peaks attributed to rutile SnO_2. For SnO_2 dosing ratios from 30 wt% to 80 wt%, only the rutile SnO_2 was formed. Figure 1 shows the XRD patterns of three SnO_2/KB composites with SnO_2 dosing ratios of 80 wt% (Fig. 1a(A)), 70 wt% (Fig. 1a(B)), and 50 wt% (Fig. 1a(C)). As mentioned above, the major phase was rutile SnO_2 overlaid by broad peaks of KB. We found that dosages of 50 wt%–80 wt% gave reasonable SnO_2/KB composites after our UC treatment. When the dosing ratio was increased from 50 wt% (Fig. 1a(C)) to 80 wt% (Fig. 1a(A)), all the XRD peaks became slightly sharper, indicating either a slight increase in the SnO_2 crystal size or an increase in crystallinity. The three broad peaks for the (110), (101), and (211) planes are in good agreement with the reported XRD results for hydrothermally synthesized SnO_2 (5–6 nm). [48,49] Assuming that the half-bandwidth of the XRD peaks depend on the crystal size, the crystallite sizes were calculated by adopting the Scherrer formula for the three planes. The calculated diameters of the SnO_2 crystallites are 2–4 nm, 3–4 nm, and 4–5 nm for the composite samples in Fig. 1a(C) (50 wt% SnO_2), 1a(B) (70 wt%), and 1a(A) (80 wt%), respectively. The sizes calculated in the three different directions were the same for all composites. This suggests that the obtained single nanocrystals of SnO_2 have spherical shapes. The proportionality of the calculated size to the SnO_2 dosing ratio (50 wt%, 70 wt%, and 80 wt%) reflects the effect of the amount of KB on the size-control of the SnO_2 particles. For dosing ratios below 50 wt%, the particle size was the same as for the dosage of 50 wt%, indicating the limit of the size-control effect of KB on SnO_2

particles. Thermogravimetric analysis (TGA) was performed on SnO_2/KB composites under an air atmosphere in order to estimate the ratio of SnO_2 and KB from the residual SnO_2 weight after oxidative decomposition of KB. Figure 1b shows TGA curves for three SnO_2/KB samples with different dosing ratios, *viz.*, 80/20 (Fig. 1b(A)), 70/30 (Fig. 1b(B)), and 50/50 (Fig. 1b(C)), and the pure KB (UC-treated KB, denoted as UC-KB, Fig. 1b(D)) as a reference. All TGA curves except that for the reference KB indicate two stages of weight loss. The initial weight loss in the temperature range of 25–200°C can be attributed to a small quantity of water and gases absorbed from the ambient. Next, the decomposition of the surface functional groups on the KB (such as lactone and carboxyl)[50] is observed at 200–400°C. The amount of oxidative decomposition of the KB can be estimated by subtracting the weight at 800 °C from that at 200 °C. The resulting SnO_2/KB ratios in the composites are found to be 75/25 (Fig. 1b(A)), 63/37 (Fig. 1b(B)), and 45/55(Fig. 1b(C)), respectively. These values are slightly lower than the respective dosing ratios. However, it is noteworthy that there are large differences in the decomposition temperature: the SnO_2-containing KB (Fig. 1b(A), (B), (C)) combusted at 430 °C, which is 170 °C lower than the UC-KB decomposition temperature (600 °C). Gao *et al*. discovered a similar shift of the combustion temperature by about 100 ˚C (decrease from 653 to 551 °C) when the pristine CNTs and TiO_2-grafted (5–10 nm particles) CNTs were combusted.[51] Other reports[49,52] have also described the same catalytic effect, which is consistent with our results.

The nanostructure of the three SnO_2/KB composites was observed by HRTEM to evaluate their morphology and crystal structure. The lower magnification images presented on the left-hand side of Figure 2 (A)–(C) show the highly dispersed SnO_2 nanodots ranging from 2 to 6 nm in

diameter within the KB matrix. The comparison of the bright-field and dark-field images clearly demonstrates the encapsulation of SnO_2 nanoparticles within the hollow structure of KB (see supporting Fig. S1). In the higher magnification HRTEM images (Fig. 2 (A)–(C), middle), one can see the more detailed nanostructure of the SnO_2, including a slight difference in the degree of crystallization among three samples. With an increase in SnO_2 dosage, the crystals seem to be more crystalline, judging from the higher contrast between the fringe and the inside of the SnO_2 nanoparticles. The SnO_2 particle size also changes depending on the dosage; the observed SnO_2 particle size is 2-4 nm for a SnO_2 content of 45 wt%, 3-5 nm for 63 wt%, and 4-6 nm for 75 wt%. The smallest particle size of 2–4 nm was obtained for the 45 wt% SnO_2 samples (Fig.2 (C)), which have a partially ambiguous slit line in the lattice arrangements as compared to those in larger SnO_2 particles such as those obtained with a 75 wt% SnO_2 content (Fig.2 (A)). In the image (Fig. 2(C)), such small and less developed particles are well attached onto the surface of a KB sphere, mostly on the inner sphere with few on the outer sphere. As is described later in Figure 3, the most optimized SnO_2/KB composite was fabricated with this dosage of 45 wt%, and the pulverization/degradation issues were completely overcome through the encapsulation of SnO_2 into the KB nest. Upon an increase of SnO_2 dosage from 45 wt% to 63 wt%, most of the SnO_2 particles remained encapsulated but seem to be slightly larger, as shown in the middle image in Fig. 2(B). The rest of the particles are attached directly on the outer spheres of the KB nests. For the 75 wt% SnO_2 composite, however, one can hardly see the KB carbon structure (Fig. 2(A), middle), while particles are enlarged to 5-6 nm and cover the whole KB matrix. The enlargement of the SnO_2 particles is consistent with the Scherrer analyses of the XRD results (Fig. 1a). Schematic illustrations are presented for each image on the right-hand side of Fig. 2.

These illustrations of three SnO_2/KB composites are also supported by the results of N_2 adsorption experiments (see supporting Fig. S2). The specific surface area (SSA) of the composites linearly decreases with a SnO_2-dosage increase from 0 wt% (pure KB) up to 67 %, while the SSA starts to slightly increase from 67 to 75 wt%. The slight increase of the SSA from 67 wt% can be due to the SnO_2 nanoparticles piled on the outer sphere of KB, as shown in Fig. 2 (A) for the 75 wt% dosage. Unlike the other two samples, this 75 wt% SnO_2 sample, which includes particles piled together on the KB outer sphere, lost the direct electronic contact between the particles and the microcrystalline graphitic carbons of the conductive KB, resulting in poor electrochemical performance (see a later section and Fig. 3).

In order to confirm the effectiveness of the highly dispersed and encapsulated structure of nanocrystalline SnO_2 in the composites for the reversible lithiation-delithiation process, the cyclability of three SnO_2/KB composites (SnO_2 = 75, 63, and 45 wt%) was tested within the potential range from 0.0 to 2.0 V (Fig. 3). The obtained results show that the cyclability of SnO_2/KB is sensitive to the dosing ratio of SnO_2 in the composites. In the case of 75 wt%-dosage (A), a capacity of 300 mAh g^{-1} was obtained at the 100th cycle, and the sample fully degraded after 170 cycles. This value is more or less consistent with the data presented in other representative recent papers (X. Li *et al.*[53], H. Song *et al.*[54], M. Alaf *et al.*[55], J. Huang *et al.*[56] , and X. Fan *et al.*[36]). Those papers reported the samples prepared with various nanocarbons (graphene and single/multi-walled CNTs) composited with loading ratios of 60–90 wt% of mostly sol-gel- or hydrothermal-derived nanosized SnO_2 particles (5-30 nm in diameter), and their best performances (400–600 mAh g^{-1} at around 0.1–0.2 C-rate) in the ranges between 50 and 200 cycles. Interestingly, a sample with a lesser dosage (63 wt%) gave the highest capacity

of a little over 800 mAh g^{-1} up to 200 cycles and was proved to be cyclable up to 700 times (see Fig. 3(B)). Most strikingly, the sample with the 45 % dosage exhibited the longest cycling performance (more than 1200 cycles), showing a gradually increasing capacity from 720 to 837 mAh g^{-1}, as shown in Figure 3(C). In fact, the 45 wt% SnO_2 composite sample showed both exceptional cycling performance (1200 cycles) and high coulombic retention (over 99%) simultaneously as shown in the inset of Fig. 3 (charge-discharge curves). Such high performance has never been attained to date, according to previous reports.[36,52-56] The reversible capacity of 837 mAh g^{-1} (at >1200 cycles) is equivalent to 1444 mAh g^{-1} relative to the mass of the SnO_2 active material, suggesting that the conversion reaction itself became reversible. This 1444 mAh g^{-1} capacity is purely ascribable to the capacity of SnO_2 in the 45 wt% dosage sample, since the capacity ascribed to the pure KB, 340 mAh g^{-1}, has already been subtracted. The KB capacity (340 mAh g^{-1}) was determined independently on the basis of a cycling test on a pristine UC-treated KB electrode (UC-KB, see supporting Fig. S3). In the case of SnO_2/KB (45:55), the capacity per SnO_2 after 1200 cycles (1444 mAh g^{-1}) was calculated from the following equation;

$$Cap._{SnO2} = (Cap._{SnO2/KB} * 1.00 - Cap._{KB} * 0.55) / 0.45$$

$Cap._{SnO2,}$, $Cap._{SnO2/KB}$, and $Cap._{SnO2/KB}$ represent the capacity purely attributed to the SnO_2 particles, the capacity per SnO_2/KB (45/55) composite (837 mAh g^{-1} at 1200th cycle), and the capacity purely attributed to the KB (340 mAh g^{-1}), respectively. These different cycling durabilities due to the different dosing ratios (SnO_2 = 45-70 wt%) can be explained by the structure of each composite. SnO_2 reacts with 8.4 lithium ions in the conversion and alloying

reaction, which causes a 359% volume expansion.[18] In addition, generation of Li_2O in the conversion reaction causes further volume expansion. Thus, during the lithiation process of SnO_2, rapid aggregation will easily occur if the sufficient distance cannot be kept among SnO_2 particles. From the results of TEM observation (Fig.2) and the N_2 adsorption experiments (see supporting Fig. S2), the SnO_2/KB composites can be classified into two groups depending on the SnO_2 loading value: one is the high-dispersion composites with highly dispersed SnO_2 nanoparticles confined within the hollow structure of KB when the SnO_2 dosage is less than 67 wt%, and the other is the outer-deposition composites with the exposed and piled SnO_2 nanoparticles outside of KB sphere when the SnO_2 dosage exceeds 67 wt%. For the outer-deposition composite with a SnO_2 dosage of 75 wt%, it is considered that the poor cycle performance has roots in the significant aggregation of SnO_2 during the lithiation, because distance between the SnO_2 nanoparticles is insufficient. By contrast, in the high-dispersion composites including 45 wt% and 63 wt% dosage, the composite structure can be maintained owing to the sufficient distance between nanoparticles.

The SEM images of the composites before and after 50 cycles for the 45 wt% and 75 wt% dosage support this postulation (see supporting Fig. S4). The sample with the 45 wt% dosage after 50 cycles maintains the fine structure of the pristine composite with a network structure containing a SEI (solid electrolyte interphase), suggesting that the reversible electrochemical reaction of SnO_2 nanoparticles occurs within the KB sphere. On the other hand, structural changes are apparent for the sample with the 75 wt% dosage, from the pristine composite to form a more uniform structure whose pores are completely filled and electrode surface are totally covered by polymeric mixture. The polymeric mixture is supposed to consist of the SEI

and the SnO_2-derived products (Sn and Li_2O). The complete covering of the composite surface by such a resistive products immediately increased the internal resistance of the system, resulting in the short cycle life with a drastic capacity decrease by 200th cycle. Thus, for the high-dispersion composite (especially with the SnO_2 dosage of 45 wt%), the total encapsulation of SnO_2 within the KB sphere keeps the SnO_2 nanoparticles from the agglomeration, as the hollow structure of KB provides some space to buffer the volume change of SnO_2 nanoparticles. Furthermore, the good contact between SnO_2 nanoparticles and the microcrystalline graphite of KB ensure the good electrical path as a composite. All of these factors enhance the cyclability of the SnO_2/KB (45/55). One interesting point is the electrochemical behavior of the SnO_2/KB (63/37) composite (Fig.3 B), showing its stable cyclability until 600th cycle but sharp capacity decrease afterwards. Comparison of charge discharge curves for SnO_2/KB (63/37) in the range of 600th and 750th (see supporting Fig.S5) highlights two exponential changes within the 150 cycles; i) disappearance of the capacity at the voltage lower than 0.4 V during lithiation process, and ii) increase of internal resistance (IR) drops at the beginning of delithiation. Both phenomena suggest that the electrochemical reaction below 0.4V including Sn alloying, lithiation of KB, and SEI formation, became largely resistive after 600th cycle. Such a sudden increase of resistance can be explained by the structure of SnO_2/KB (63/37) composite. As shown in HRTEM observation (Fig.2 B) shows that some of SnO_2 nanoparticles are exposed and attached directly on the outer spheres of the KB. These several "outer" SnO_2 nanoparticles can reversibly react owing to the good contact on the conductive KB carbon, even though the SEI and Li_2O gradually accumulates around the "outer" particles. After certain cycle time such as 600 cycles, however, these locally accumulated products start to link each other and to cover

the whole entity of KB spheres including encapsulated SnO_2. The totally covered SnO_2/KB spheres lost the connection from the conductive carbon network, resulting in a large increase of resistivity and sharp capacity decrease. This result also demonstrates the importance of the optimized encapsulation of SnO_2 in the hollow KB structure, achieved by the SnO_2 dosage of 45 wt% in this report, to accomplish an anomalous long cycle life over 1200 cycles. The other interesting phenomenon shown in Fig. 3(C) is the gradual capacity rise during cycling by ca. 1 mAh g^{-1} (composite) per each 10 cycles, which is rarely observed in electrodes made of intercalation compounds such as $LiCoO_2$, $LiMn_2O_4$, and $Li_4Ti_5O_{12}$. However, there are many reports of capacity rises in the conversion reactions of metal oxide anode materials such as Fe_2O_3, Cu_2O, and MnO_2.[57-59]

In order to obtain further information on the lithiation/delithiation processes for our composites, cyclic voltammetry was performed for the pure KB (UC-treated KB, denoted as UC-KB), SnO_2/KB (75/25), and SnO_2/KB (45/55) (see supporting Fig. S6). For the UC-KB (Fig. S6 (A)), a strong cathodic peak was observed around 0.7 V during the first lithiation process, which corresponds to the formation of the SEI layer on the external surface of the KB. The following peaks observed at 0.3, 0.1, and 0.0 V correspond to the SEI formation as well as the Li^+ intercalation between the graphene layers of KB.[60,61] For the SnO_2/KB composites with 75 wt% and 45 wt% dosages (see supporting Fig. S6 (B) and (C)), there are characteristic cathodic peaks at 0.9, 0.7, and 0.0 V, corresponding to the conversion reaction of SnO_2, SEI layer formation on KB, and the alloying reaction of Sn ($xLi^+ + Sn + xe^- \rightarrow Li_xSn$ (x = 0-4.4)) and Li^+ intercalation into KB graphene layers, respectively. During the anodic sweep (delithiation process), two peaks were observed around 0.5 and 1.3 V. The peak at 0.5 V represents the

dealloying of Li_xSn (x = 0-4.4).[14] The other oxidation peak around 1.3 V can be considered to be due to the conversion reaction. In recent years, there have been some reports mentioning that the conversion reaction of SnO_2 becomes reversible in the case of small particles. [23,41] Although these phenomena are not fully elucidated yet, Tarascon *et al*. suggested that the key to the reversibility of the conversion of transition metal oxides or other metal oxides with Li^+ is the electrochemically driven formation of highly reactive metallic nanoparticles during the first lithiation process, which enables the reversible formation/decomposition of Li_2O upon subsequent cycles.[62] The reversible oxidation peak around 1.3 V observed for our composites supports those reports. Compared to the sample with the 45 wt% dosage, the sample with the 75 wt% dosage exhibits different CV results (see supporting Fig. S6 (B)). During the 1st cycle, the voltages of the main peaks observed for the sample with the 75 wt% dosage are more or less the same as those observed for the 45 wt% dosage, while the contribution of peaks attributed to the KB became less pronounced. From the second cycle, the electrode with the 75 wt% dosage shows significant deterioration in its cyclic voltammogram, which is in very good agreement with the results of the cycling tests (see Fig. 3 (A)).

An optimized SnO_2/KB (45/55) composite exhibited a reversible discharge capacity at a steady-state cycling. For example, at 10^{th} cycle, the 45 wt% dosage composite showed 792 mAh g^{-1} relative to the mass of the composite, which is equivalent to 1347 mAh g^{-1} relative to the mass of the SnO_2. Such a large capacity is very close to the theoretical capacity of SnO_2 including both the alloying and conversion process (1494 mAh g^{-1}), rather than the alloying process alone (783 mAh g^{-1}). However, it remains unclear whether the conversion reaction really becomes reversible. In order to answer this question, we tried to quantify the degree of

reversibility of the SnO_2 conversion reaction for our composites by determining the number of reaction electrons from the cyclic voltammogram (Fig. 4a). To evaluate the electron numbers, we assumed that the oxidation peak below 1.0 V is attributed to the alloying process and the other peak over 1.0 V is attributed to the conversion process. From the deconvolution of the cyclic voltammogram into two peaks and the comparison of their areas, the electron numbers for both reactions were evaluated. The evaluated electron numbers were found to be 4.76 for the alloying reaction and 2.82 for the conversion reaction. Thus, the reaction could be formulated as follows,

Conversion reaction : $SnO_{1.41} + 2.82\ Li^+ + 2.82\ e^- \rightleftarrows Sn + 1.41Li_2O$ (1–2 V)

Alloying reaction : $Sn + 4.76\ Li^+ + 4.76\ e^- \rightleftarrows Li_{4.76}Sn$ (0–1 V)

Total reaction : $SnO_{1.41} + 7.58\ Li^+ + 7.58\ e^- \rightleftarrows Li_{7.58}SnO_{1.41}$ (0–2 V)

Furthermore, in order to verify the postulated formula from the spectroscopic measurements, the electronic state and local structure of Sn was investigated by performing *in-situ* X-ray absorption fine structure (XAFS) measurements during the 1st and 10th cycles. Figure 4b-e shows the X-ray absorption near-edge structure (XANES) spectra of the Sn K edge for the SnO_2/KB(45/55) composites during the 1st lithiation (Fig. 4b) and delithiation (Fig. 4c). The Sn K-edge spectra include information about the transition from 1*s* to the 5*p* unoccupied orbital. During the lithiation and delithiation of Sn compounds, the electron transfer occurs to and from the 5*p* orbital. Accordingly, the integrated area of the Sn K-edge spectrum shows the numbers of electrons, *i.e.*, the valence state, of the Sn atoms in its compounds. In this article, the parameter for determining the valence state is defined as the “formal valence number”, which is calculated

from the relative ratio of the integrated area of the Sn K-edge spectrum obtained for our composite and for reference materials (SnO_2, Sn, and $Li_{4.4}Sn$). For example, the formal valence number of $Li_{4.4}Sn$ is written as 4.4-. The Sn K-edge spectra of SnO_2 and Sn foil are used as references for Sn(4+) and Sn(0), respectively. Fig. 4f shows the formal valence number of Sn in the 1st cycle. During the lithiation process from potentials (A) to (F), the valence state decreased from (4.0+) to (4.3-). The valence state reaches zero around 0.5 V and continues to decrease to -4.3 from 0.5 down to 0 V. The negative value of the Sn valence state indicates that the electron density of Sn atoms exceeds the inherent Sn electron density because of the alloying reaction between lithium and tin metal. During the 1st delithiation, the valence state linearly increases as a function of the voltage (from (F) to (K)). Such a valence change with a large hysteresis between lithiation and delithiation process is analogous to the shape of the charge-discharge curve of uc-SnO_2/KB (45:55) as shown in the inset of Fig.3. The large hysteresis between 1st lithiation and delithiation can be due to the large electromotive force to decompose Li_2O[63] and the large difference in mobility that is expected between Sn cations and Li^+ [64]. Eventually, the formal valence number of Sn reaches 3.1+ at 2.0 V (K). This indicates that the Sn in this composite did not completely recover to its initial state (4.0+) during the conversion reaction in the 1st cycle. Figure 4 d and e show the changes in the Sn K-edge XANES spectra of the 45 wt%-dosage composite during the 10th cycle. Fig. 4g shows the formal valence number of Sn in the 10^{th} cycle calculated from the spectra of Fig.4 d and e. It can be seen that the formal valence number of Sn recovers almost perfectly during the 10th lithiation-delithiation cycle, as the valence decreases from 3.2+ (L) to 4.4- (P) and then recovers to 2.9+ (T). To summarize the results of the XANES spectra at 10^{th} cycle, the reaction formula

can be written as follows.

Conversion reaction : $SnO_{1.45} + 2.9\ Li^+ + 2.9\ e^- \rightleftarrows Sn + 1.45Li_2O$

Alloying reaction : $Sn + 4.4\ Li^+ + 4.4\ e^- \rightleftarrows Li_{4.4}Sn$

Total reaction : $SnO_{1.45} + 7.3\ Li^+ + 7.3\ e^- \rightleftarrows Li_{7.3}SnO_{1.45}$

The electron numbers obtained from the cyclic voltammetry and *in-situ* XAFS measurements are in very good agreement for all three reactions (conversion, alloying, and total reactions). Thus, the reversibility of the conversion reaction for our SnO_2/KB composite was verified by both electrochemical and spectroscopic studies.

Figure 5 shows HRTEM images of the as-prepared SnO_2/KB (45/55) composite (a), the composite at 2.0 V (delithiated) after 10 cycles (b), and the composite at 0.0 V (lithiated) after 10 cycles (c). Before cycling, one can clearly see that the nanosized SnO_2 particles of 2–4 nm are attached onto the surface of KB, mostly on its inner spheres (Fig. 5a). After 10 cycles, the overall morphology of the composite changed. The HRTEM image taken at 2.0 V after the 10th cycle (Fig. 5b) shows two phases in the composites: a transparent uniform phase and a phase with dispersed dots. The former is thought to consist of the SEI layer and the lithium-intercalated graphene layers of KB. The latter can be the particles of Sn spiecies, which mostly have diameters of 5 nm and are well attached to the inner sphere of the KB. Since the HRTEM images of the as-prepared composite show SnO_2 particles with a diameter of 3 nm (Fig. 5a), the spherical particle volume has increased by a factor of three after 10 cycles. The disappearance of the crystal lattice in the HRTEM images and the ring in the electron diffraction

images (Fig. 5b inset) suggest that all the crystalline SnO_2 particles have become amorphous. Interestingly, the HRTEM images taken at 0.0 V after 10 cycles (Fig. 5c) show that the SnO_2 particle size (5 nm) remains unchanged during the lithiation process in the 10th cycle, even though the alloying and conversion reaction occurs from 2.0 to 0.0 V. In contrast, large SnO_2 particles (for example, with a diameter of 100 nm) deteriorate from the 1st cycle and are transformed into 10 nm Sn particles dispersed within the large volume of Li_2O during its conversion and alloying reaction (see supporting Fig. S7). This morphology change results in the phase separation of Sn and stable Li_2O. On the other hand, the SnO_2 particle size for our as-prepared composite is about 3 nm, as seen in the HRTEM images. In this case, the estimated thickness of Li_2O formed around the Sn particles during conversion reaction can be remarkably thin, consisting of only 1–2 Li_2O molecular layers on the surfaces of the small Sn particles (< 3 nm). Such an extremely thin Li_2O layer is unstable and is almost impossible to exist because of its high surface energy of Li_2O on Sn metal nanoparticles. Thus, the SnO_2 in our composites after the lithiation (Fig. 5c) possesses a blended amorphous structure like a solid-solution of tin, oxygen, and lithium, such as "$Li_xSnO_{1.45}$ (x= 0 – 7.3)," as illustrated in Fig. 6, instead of separated Sn and Li_2O. In this condition, the smooth valence change of Sn can proceed by maintaining the appropriate bond length of Sn-Li and Sn-O without forming Li_2O. Such a peculiar reaction can avoid the thermodynamic barrier of Li_2O and provide reverse and smooth lithiation and delithiation of Sn species. Thus, this speculated $Li_xSnO_{1.45}$, which is highly dispersed in the KB matrix, could facilitate the reversible alloying and conversion reactions without its deterioration even after 1200 cycles.

Our last question is about the structure of this blended amorphous structure ($Li_xSnO_{1.45}$). As

shown in the insets of Fig.5b and c, the electron diffraction observation of the SnO_2/KB (45/55) after 10 cycles confirms that this sphere does not have a long-range ordered structure (> 1 nm). In order to investigate the short-range order of the average local coordination environment around the Sn atom within a diameter of 4 Å, we performed extended X-ray absorption fine structure (EXAFS) analysis using the results of the *in-situ* XAFS measurement. The spectra obtained for the as-prepared composites at the open-circuit voltage (OCV; Fig. 7a (A)) shows a strong peak at 1.6 Å derived from Sn-O bonding, which corresponds well with previous reports.[65] As the voltage decreases, this peak at 1.6 Å decreases and finally disappears at 0.0 V. In addition, it is confirmed that a new weak peak due to Sn-Sn bonding appeared around 2.7 Å at 0.2 V, and this peak also disappeared at 0.0 V (F). Then, as the voltage increases between 0.0 V (F) and 2.0 V (L), the Sn metal peak (2.7 Å) and SnO_2 peak (1.6 Å) reappear at 0.3 V and 0.8 V, respectively. The disappearance and reappearance of these two peaks were also observed at the 10th cycle (Fig. 7b), indicating the reversible rearrangement of the short-range structure of $Li_xSnO_{1.45}$. These results suggest that the $Li_xSnO_{1.45}$ possesses an amorphous structure in terms of long-range order (>1 nm), but a relatively ordered short-range structure (<4 Å). This short-range structure can be rearranged owing to the reversible exchange of the oxygen atoms between Sn and Li, resulting in the repeated disappearance and reappearance of the two peaks (Sn-O and Sn-Sn) with the voltage changes.

Conclusions

We successfully prepared a novel UC-treated SnO_2/KB composite that readily transforms into a blended amorphous structure composed of $Li_xSnO_{1.45}$ (x: 0–7.3) completely encapsulated within

the hollow-structured KB. The SnO_2/KB composite with the optimized SnO_2 dosage of 45 wt% exhibits a high reversible capacity of 837 mAh g^{-1} relative to the composite mass (1444 mAh g^{-1} relative to SnO_2 mass after subtracting the capacity attributed to the KB in the composite) over 1200 cycles. Such an anomalous cycle life was achieved owing to a peculiar nanostructure that enables the existence of the multiple phases of Sn, Li, O, and C (KB) species. This novel multiphase material is a model case of SnO_2 to overcome conversion essentials, i.e., reversible conversion reactions can be achieved by the complete encapsulation of SnO_2.

Acknowledgements

The synchrotron radiation experiments were performed at Spring-8 with the approval of the Japan Synchrotron Radiation Research Institute (JASRI). This work was supported by JSPS KAKENHI Grant Number 25249140. The authors would like to appreciate Dr. Miyamoto for his helps in XRD and N_2 adsorption measurements and Prof. P. Simon for his advise on the manuscript.

Notes and references

1. M. Armand and J. M. Tarascon, *Natur*, 2008, **451**, 652-657.
2. M. Yoshio, H. Y. Wang, K. Fukuda, Y. Hara and Y. Adachi, *J. Electrochem. Soc.*, 2000, **147**, 1245-1250.
3. L. Zeng, C. Zheng, J. Xi, H. Fei and M. Wei, *Carbon*, 2013, **62**, 382-388.
4. Y. Liu, X. Zhao, F. Li and D. Xia, *Electrochim. Acta*, 2011, **56**, 6448-6452.
5. D. Yonekura, E. Iwama, N. Ota, M. Muramatsu, M. Saito, Y. Orikasa, W. Naoi and K. Naoi, *PCCP*, 2014, **16**, 6027-6032.
6. M. F. Hassan, Z. Guo, Z. Chen and H. Liu, *Mater. Res. Bull.*, 2011, **46**, 858-864.
7. P. Lian, X. Zhu, H. Xiang, Z. Li, W. Yang and H. Wang, *Electrochim. Acta*, 2010, **56**, 834-840.
8. H. Qiao, L. Xiao, Z. Zheng, H. Liu, F. Jia and L. Zhang, *J. Power Sources*, 2008, **185**, 486-491.

9. H. Kim, D.-H. Seo, S.-W. Kim, J. Kim and K. Kang, *Carbon*, 2011, **49**, 326-332.
10. X. H. Huang, J. P. Tu, C. Q. Zhang, X. T. Chen, Y. F. Yuan and H. M. Wu, *Electrochim. Acta*, 2007, **52**, 4177-4181.
11. H. Wang, Q. Pan, J. Zhao and W. Chen, *J. Alloys Compd.*, 2009, **476**, 408-413.
12. X. H. Huang, X. H. Xia, Y. F. Yuan and F. Zhou, *Electrochim. Acta*, 2011, **56**, 4960-4965.
13. M. F. Hassan, Z. P. Guo, Z. Chen and H. K. Liu, *J. Power Sources*, 2010, **195**, 2372-2376.
14. S. Oro, K. Urita and i. moriguchi, *Chem. Commun.*, 2014.
15. B. Guo, J. Shu, Z. Wang, H. Yang, L. Shi, Y. Liu and L. Chen, *Electrochem. Commun.*, 2008, **10**, 1876-1878.
16. R. A. Huggins, *Solid State Ionics*, 1998, **113**, 57-67.
17. W. J. Zhang, *J. Power Sources*, 2011, **196**, 13-24.
18. I. A. Courtney and J. R. Dahn, *J. Electrochem. Soc.*, 1997, **144**, 2045-2052.
19. M. Winter and J. O. Besenhard, *Electrochim. Acta*, 1999, **45**, 31-50.
20. P. A. Conner and J. T. S. Irvine, *J. Power Sources*, 2001, **97-8**, 223-225.
21. M. Mohamedi, S.-J. Lee, D. Takahashi, M. Nishizawa, T. Itoh and I. Uchida, *Electrochim. Acta*, 2001, **46**, 1161-1168.
22. D. Kim, D. Lee, J. Kim and J. Moon, *Acs Applied Materials & Interfaces*, 2012, **4**, 5408-5415.
23. K. Ui, S. Kawamura and N. Kumagai, *Electrochim. Acta*, 2012, **76**, 383-388.
24. C. J. Wen and R. A. Huggins, *J. Electrochem. Soc.*, 1981, **128**, 1181-1187.
25. L. Y. Beaulieu, K. W. Eberman, R. L. Turner, L. J. Krause and J. R. Dahn, *Electrochem. Solid-State Lett.*, 2001, **4**, A137-A140.
26. T. Brousse, S. M. Lee, L. Pasquereau, D. Defives and D. M. Schleich, *Solid State Ionics*, 1998, **113**, 51-56.
27. Y. Wang and J. Y. Lee, *Electrochem. Commun.*, 2003, **5**, 292-296.
28. Y. Wang and J. Y. Lee, *J. Power Sources*, 2005, **144**, 220-225.
29. Q. Fan, P. J. Chupas and M. S. Whittingham, *Electrochem. Solid-State Lett.*, 2007, **10**, A274-A278.
30. J. S. Chen and X. W. Lou, *Small*, 2013, **9**, 1877-1893.
31. L. Yuan, K. Konstantinov, G. X. Wang, H. K. Liu and S. X. Dou, *J. Power Sources*, 2005, **146**, 180-184.
32. Y. Liang, J. Fan, X. Xia and Z. Ha, *Mater. Lett.*, 2007, **61**, 4370-4373.
33. J. S. Chen, Y. L. Cheah, Y. T. Chen, N. Jayaprakash, S. Madhavi, Y. H. Yang and X. W. Lou, *J. Phys. Chem. C*, 2009, **113**, 20504-20508.
34. J. Wang, D. Li, X. Fan, L. Gou, J. Wang, Y. Li, X. Lu and Q. Li, *J. Alloys Compd.*, 2012, **516**, 33-37.
35. S. Nam, S. Kim, S. Wi, H. Choi, S. Byun, S.-M. Choi, S.-I. Yoo, K. T. Lee and B. Park, *J. Power Sources*, 2012, **211**, 154-160.
36. X.-Y. Fan, X.-Y. Shi, J. Wang, Y.-X. Shi, J.-J. Wang, L. Xu, L. Gou and D.-L. Li, *J. Solid State Electrochem.*, 2013, **17**, 201-208.

37. D. Ahn, X. Xiao, Y. Li, A. K. Sachdev, H. W. Park, A. Yu and Z. Chen, *J. Power Sources*, 2012, **212**, 66-72.
38. L. Zhang, G. Zhang, H. B. Wu, L. Yu and X. W. Lou, *Adv. Mater.*, 2013, **25**, 2589-2593.
39. H. N. Lim, R. Nurzulaikha, I. Harrison, S. S. Lim, W. T. Tan, M. C. Yeo, M. A. Yarmo and N. M. Huang, *Ceram. Int.*, 2012, **38**, 4209-4216.
40. B. Zhao, G. H. Zhang, J. S. Song, Y. Jiang, H. Zhuang, P. Liu and T. Fang, *Electrochim. Acta*, 2011, **56**, 7340-7346.
41. X. Zhou, L.-J. Wan and Y.-G. Guo, *Adv. Mater.*, 2013, **25**, 2152-2157.
42. H. Song, N. Li, H. Cui and C. Wang, *J. Mater. Chem. A*, 2013, **1**, 7558-7562.
43. K. Naoi, S. Ishimoto, N. Ogihara, Y. Nakagawa and S. Hatta, *J. Electrochem. Soc.*, 2009, **156**, A52-A59.
44. K. Naoi, S. Ishimoto, Y. Isobe and S. Aoyagi, *J. Power Sources*, 2010, **195**, 6250-6254.
45. https://www.lion.co.jp/en/chem/product/carbon/carbon01.htm
46. R. P. Hjelm, W. A. Wampler, P. A. Seeger and M. Gerspacher, *J. Mater. Res.*, 1994, **9**, 3210-3222.
47. http://www.spring8.or.jp/wkg/BL14B2/instrument/lang-en/INS-0000001471/view
48. J. Zhu, D. Wang, L. Wang, X. Lang and W. You, *Electrochim. Acta*, 2013, **91**, 323-329.
49. H. Liu, D. Long, X. Liu, W. Qiao, L. Zhan and L. Ling, *Electrochim. Acta*, 2009, **54**, 5782-5788.
50. H. Oda, *TANSO*, 2008, **2008**, 296-306.
51. B. Gao, C. Peng, G. Z. Chen and G. L. Puma, *Appl. Catal., B*, 2008, **85**, 17-23.
52. Z. Du, X. Yin, M. Zhang, Q. Hao, Y. Wang and T. Wang, *Mater. Lett.*, 2010, **64**, 2076-2079.
53. J. Liu, J. Huang, X. Li, H. Liu and Y. Zhang, *Mater. Sci. Semicond. Process.*, 2013, **16**, 742-746.
54. H. K. Zhang, H. H. Song, X. H. Chen, J. S. Zhou and H. J. Zhang, *Electrochim. Acta*, 2012, **59**, 160-167.
55. M. Alaf, D. Gultekin and H. Akbulut, *Appl. Surf. Sci.*, 2013, **275**, 244-251.
56. J. Liu, J. Huang, L. Hao, H. Liu and X. Li, *Ceram. Int.*, 2013.
57. M. F. Hassan, Z. Guo, Z. Chen and H. Liu, *Mater. Res. Bull.*, 2011, **46**, 858-864.
58. C. Chen, N. Ding, L. Wang, Y. Yu and I. Lieberwirth, *J. Power Sources*, 2009, **189**, 552-556.
59. Y. Wang, Z. J. Han, S. F. Yu, R. R. Song, H. H. Song, K. Ostrikov and H. Y. Yang, *Carbon*, 2013, **64**, 230-236.
60. C. S. Wang, G. T. Wu and W. Z. Li, *J. Power Sources*, 1998, **76**, 1-10.
61. J. R. Dahn, T. Zheng, Y. Liu and J. S. Xue, *Science*, 1995, **270**, 590-593.
62. J. M. Tarascon, S. Grugeon, M. Morcrette, S. Laruelle, P. Rozier and P. Poizot, *C. R. Chim*, 2005, **8**, 9-15.
63. J. Ma, W.-Y. Liu, C.-L. Li and Z.-W. Fu, *Electrochim. Acta*, 2006, **51**, 2030-2041.
64. R. E. Doe, K. A. Persson, Y. S. Meng and G. Ceder, *Chem. Mater.*, 2008, **20**, 5274-5283.
65. A. N. Mansour, S. Mukerjee, X. Q. Yang and J. McBreen, *J. Synchrotron Radiat.*, 1999, **6**, 596-598.

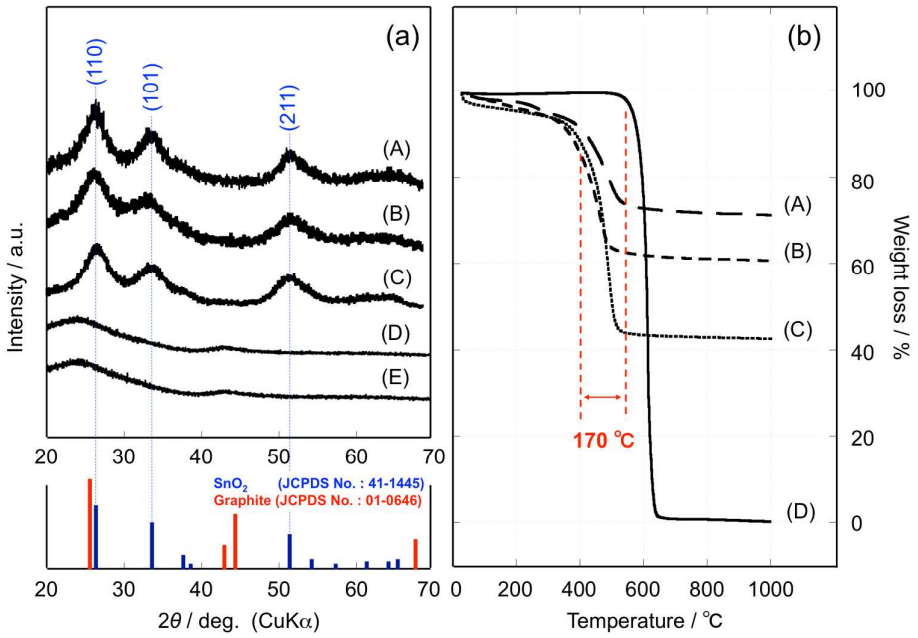

Figure 1. (a) XRD patterns obtained for UC-treated nc-SnO_2/KB composites with various dosing ratios: (A) SnO_2/KB = 80/20 by mass (75/25, calculated from results of TGA shown in Fig. 1(b)), (B) SnO_2/KB = 70/30 (63/37), and (C) SnO_2/KB = 50/50 (45/55). Patterns for (D) UC-treated KB (UC-KB) and (E) pristine KB (UC-untreated) are shown for reference. All three SnO_2/KB composites have three broad peaks at 2θ = 27°, 34°, and 52°, corresponding to the (110), (101), and (211) planes for the tetragonal rutile structure (space group *P*42/*mnm*) of SnO_2 (blue: JCPDS No. 41-1445). The XRD patterns for the UC-KB and pristine KB have identical characteristic peaks at 24° and 42° that are shifted to lower angles from the respective (002) and (10L) planes for the hexagonal structure (space group P63/mmc) of graphite (red: JCPDS No. 01-0646).

(b) TGA curves for UC-treated nc-SnO_2/KB composites prepared with the same dosing ratios as in Figure 1: (A) SnO_2/KB = 75/25, (B) SnO_2/KB = 63/37, (C) SnO_2/KB = 45/55. The curve for (D) UC-treated KB (UC-KB) is shown for reference. The measurements were performed at a sweep rate of 5°C min^{-1} from ambient temperature to 1000 ˚C under a synthetic air atmosphere.

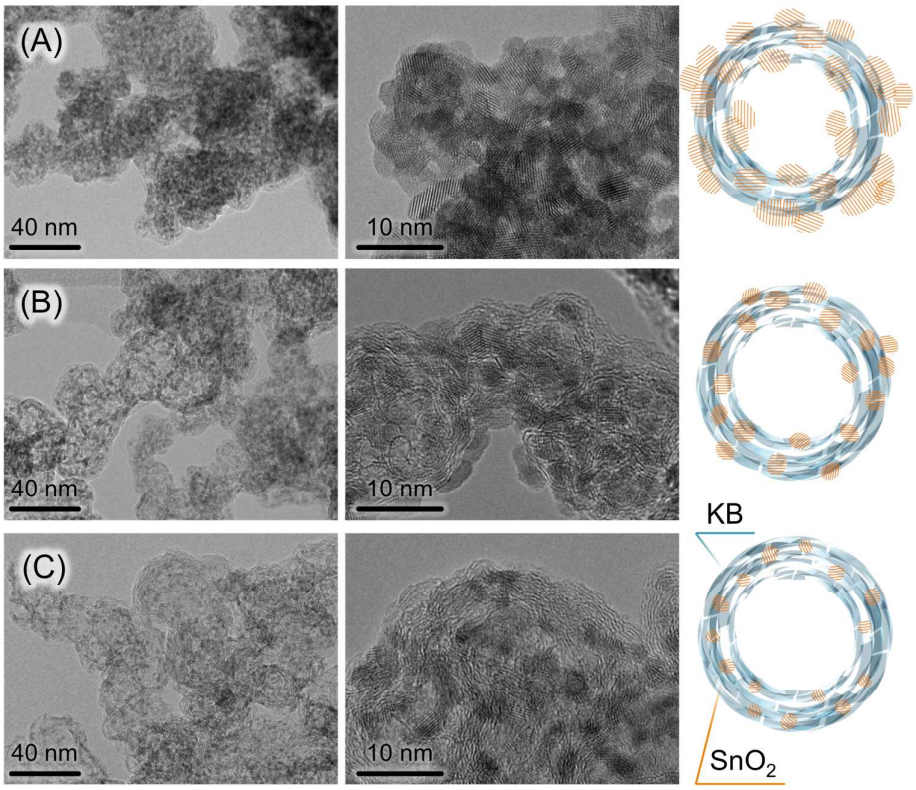

Figure 2. HRTEM images (left; low magnification, middle; high magnification) of the composite formation for (A) SnO_2/KB = 75/25, (B) SnO_2/KB = 63/37, and (C) SnO_2/KB = 45/55, as in Figures 1. Schematic illustrations are presented for each image on the right-hand side. The magnified HETEM views (middle) for the composites show a clear dependency between the degree of the dispersion and the particle sizes of the UC -formed SnO_2 within the hollow structure of KB after the UC treatment. The relation between the SnO_2 dosing ratio for the SnO_2/KB compounds and their specific surface area is shown in Fig S1.

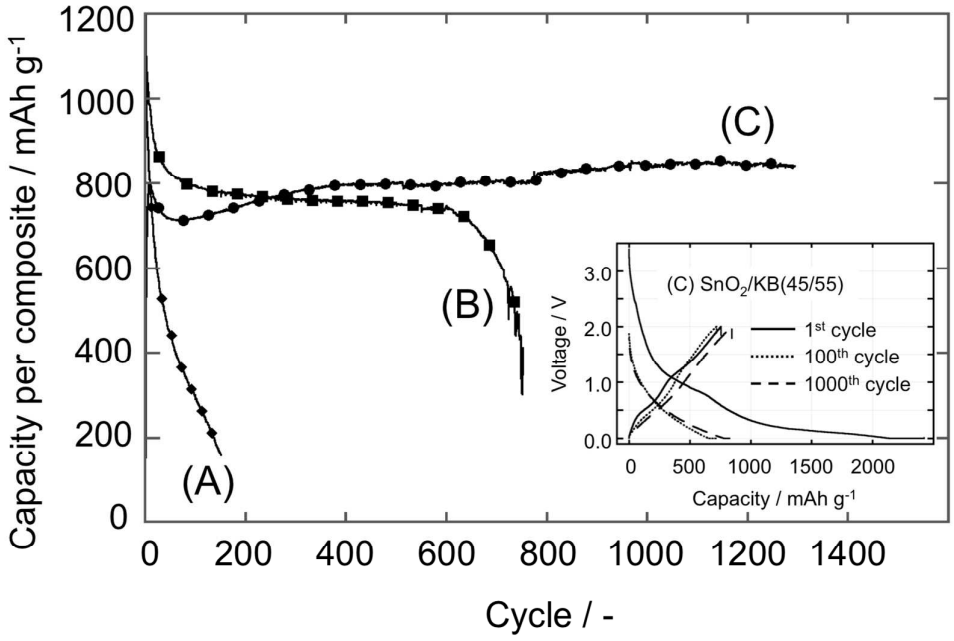

Figure 3. Cycling performance for three UC-treated nc-SnO_2/KB composites with various dosing ratios: (A) SnO_2/KB = 75/25 (by mass), (B) SnO_2/KB = 63/37, and (C) SnO_2/KB = 45/55. The cycling test was performed on half-cells consisting of Li/1 M $LiPF_6$ (EC+DEC)/UC-SnO_2/KB in the CC-CV (lithiation) and CC (delithiation) mode between 0.0 and 2.0 V at a current density of 300 mA/g (0.2 C). The inset figure shows the charge-discharge curves at 1st, 100th, and 1000th cycle for the composite (C) SnO_2/KB = 45/55. The large irreversible capacity is mainly due to the reaction on the KB (see supporting Fig. S2)

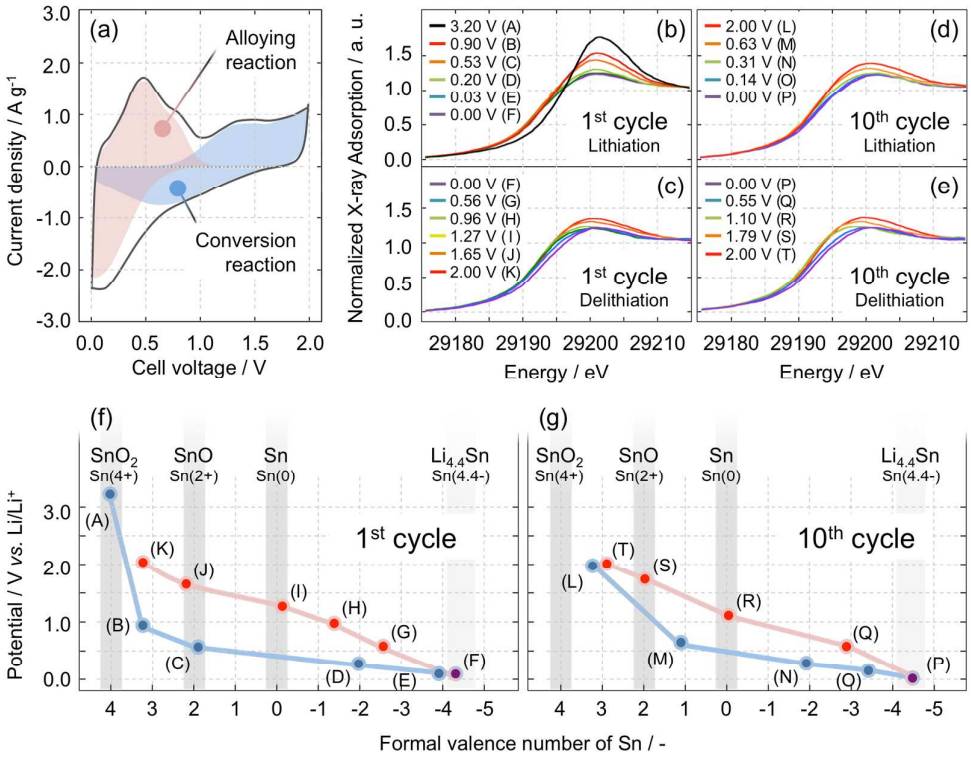

Figure 4. **Top:** (a) Cyclic voltammogram of SnO_2/KB composite after 10 cycles and (b)-(e) normalized Sn K-edge XANES absorption spectra in the range of 29185–29215 eV for the Li_xSnO_2 system with electrochemically inserted/deinserted lithium ions during 1st and 10th cycle. Spectra (b) corresponds to the1st lithiation, (c) to the 1st delithiation, (d) to the 10th lithiation, and (e) to the 10th delithiation process. **Bottom:** Changes in the evaluated "formal valence number" of Sn during the lithiation-delithiation process (vs. Li/Li^+) for the (f) 1st cycle and (g) 10th cycle. The formal valence number of Sn for the composites was calculated from the following equations; in the case of 1) the formal valence number is above Sn, V = ((A – A(Sn))/(A(SnO_2) – A(Sn))*V(SnO_2), 2) the formal valence number is below Sn, V= ((A(Sn)-A)/(A(Sn)-A($Li_{4.4}Sn$))*V($Li_{4.4}Sn$). V: the formal valence number , A: integrated area of the Sn K-edge spectrum.

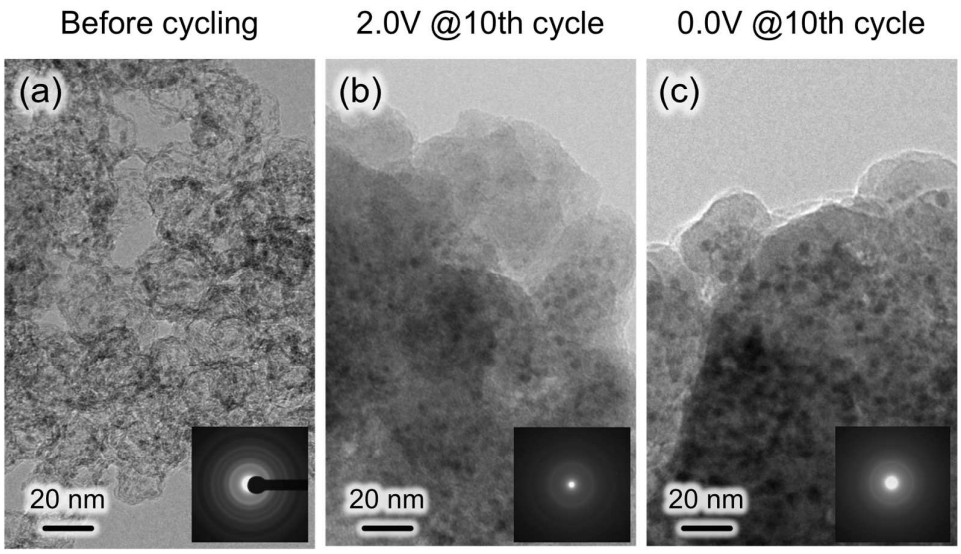

Figure 5. HRTEM images of SnO_2/KB = 45/55 composite (a) before cycling, (b) after 10 cycles at 2.0 V (delithiated), and (c) after 10 cycles at 0.0 V (lithiated). Before cycling, ultrafine (2–4 nm) SnO_2 particles are encapsulated within the hollow structure of KB. After cycling at 2.0 V and 0.0 V, the HRTEM images show 5 nm spherical shapes covered with a diffuse polymeric phase, possibly an SEI film. The corresponding SAED patterns of the SnO_2/KB composite before cycling, at 2.0 V, and at 0.0 V are shown as insets in (a), (b), and (c), respectively.

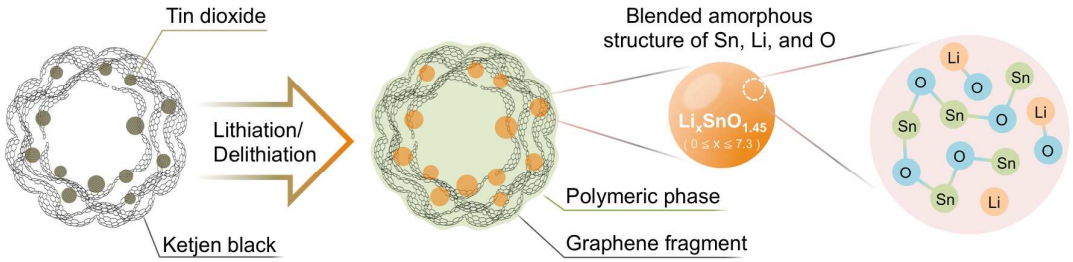

Figure 6. Illustration of the material transformation from the as-prepared SnO_2/KB nanocomposites into the blended amorphous structure "$Li_xSnO_{1.45}$ (x=0-7.3)" after repeated lithiation and delithiation processes, typically 10 cycles. The proposed new species "$Li_xSnO_{1.45}$ (x=0-7.3)" is still well-confined within the hollow structure of KB which are filled and covered by polymeric phases (possibly SEI). The steady-state redox is maintained over 1200 cycles with a slight increase of capacity (1 mAh g^{-1} per 10 cycles).

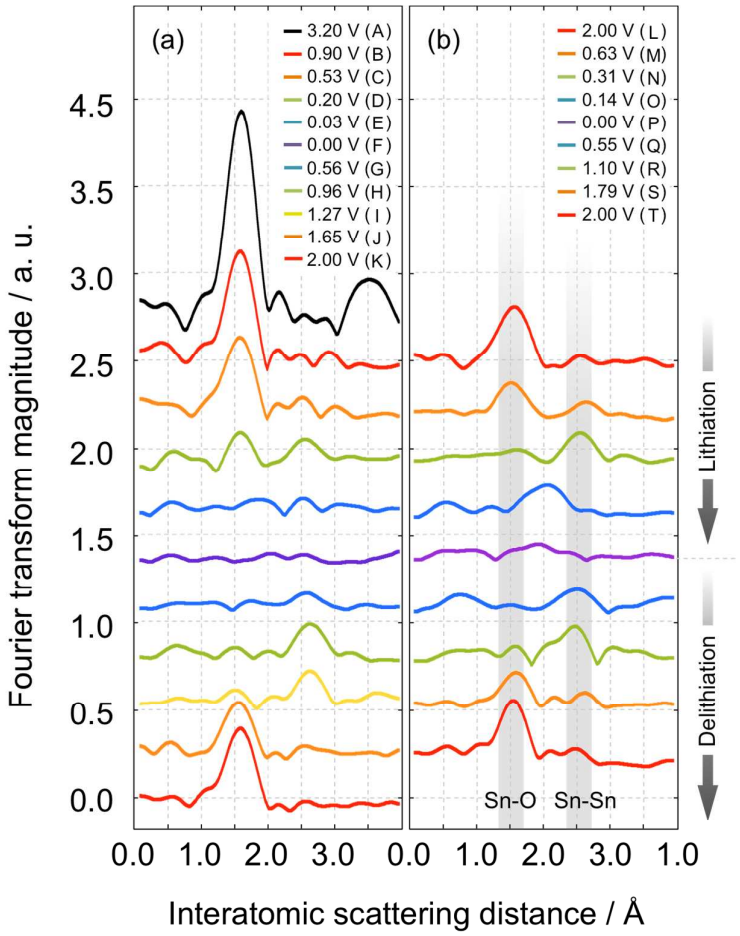

Figure 7. Fourier transforms of the k^3-weighted Sn K-edge EXAFS spectra taken during the charge cycle as a function of the voltage for the (a) 1st lithiation and delithiation, and (b) 10th lithiation and delithiation processes. The Fourier transform range is 2.05–11.1 $Å^{-1}$.

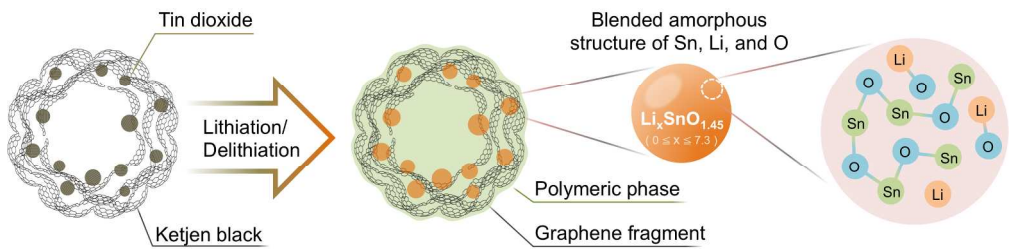

Illustration of the material transformation from the as-prepared SnO_2/KB nanocomposites into the blended amorphous structure "$Li_xSnO_{1.45}$ (x=0-7.3)" after repeated lithiation and delithiation processes, typically 10 cycles. The proposed new species "$Li_xSnO_{1.45}$ (x=0-7.3)" is still well-confined within the hollow structure of KB which are filled and covered by polymeric phases (possibly SEI). The steady-state redox is maintained over 1200 cycles with a slight increase of capacity (1 mAh g^{-1} per 10 cycles).
431x105mm (150 x 150 DPI)